Characteristic lengths affecting evaporative drying of porous media

Peter Lehmann,[1] Shmuel Assouline,[2,*] and Dani Or[1]

[1]*School of Architectural, Civil and Environmental Engineering (ENAC), Laboratory of Soil and Environmental Physics (LASEP),*
Ecole Polytechnique Fédérale de Lausanne (EPFL), Switzerland
[2]*Institute of Soil, Water and Environmental Sciences, A.R.O., Volcani Center, Israel*

Evaporation from porous media involves mass and energy transport including phase change, vapor diffusion, and liquid flow, resulting in complex displacement patterns affecting drying rates. Force balance considering media properties yields characteristic lengths affecting the transition in the evaporation rate from a liquid-flow-based first stage limited only by vapor exchange with air to a second stage controlled by vapor diffusion through the medium. The characteristic lengths determine the extent of the hydraulically connected region between the receding drying front and evaporating surface (film region) and the onset of flow rate limitations through this film region. Water is displaced from large pores at the receding drying front to supply evaporation from hydraulically connected finer pores at the surface. Liquid flow is driven by a capillary pressure gradient spanned by the width of the pore size distribution and is sustained as long as the capillary gradient remains larger than gravitational forces and viscous dissipation. The maximum extent of the film region sustaining liquid flow is determined by a characteristic length L_C combining the gravity characteristic length L_G and viscous dissipation characteristic length L_V. We used two sands with particle sizes 0.1–0.5 mm ("fine") and 0.3–0.9 mm ("coarse") to measure the evaporation from columns of different lengths under various atmospheric evaporative demands. The value of L_G determined from capillary pressure-saturation relationships was 90 mm for the coarse sand and 140 mm for the fine sand. A significant decrease in drying rate occurred when the drying front reached the predicted L_G value (viscous dissipation was negligibly small in sand and $L_C \approx L_G$). The approach enables a prediction of the duration of first-stage evaporation with the highest water losses from soil to the atmosphere.

I. INTRODUCTION

Drying of porous media is characterized by the invasion of a gaseous phase replacing the evaporating liquid and the formation of a drying front—i.e., an interface separating the liquid-saturated zone and partially air-filled region. Evaporation is a key process for water exchange between soil and atmosphere; it is involved in the plant physiological function through transpiration and affects the amount of available water for plants and microorganisms inhabiting the soil. Drying processes are of significant industrial and engineering importance including food processing and preservation, production of ceramics and paper, eye and skin care, and numerous construction activities. Notwithstanding the prominent role of drying in many applications, prediction of drying rates from porous media remains a challenge. The evaporation rate is affected by both atmospheric demand (humidity, temperature, and velocity of ambient air) and by porous-medium pore space and transport properties (thermal and hydraulic conductivities and vapor diffusion). Consequently, complex and highly dynamic interactions between medium properties, transport processes, and boundary conditions result in a wide range of evaporation behaviors as discussed by Van Brakel and Prat and will be elaborated on in what follows [1,2].

A. Different stages of evaporative drying

Focusing on the effects of soil properties on evaporation behavior, it is customary and convenient to scale the actual evaporation rate e by the potential evaporation rate e_0 under similar conditions from a free water surface. The relative drying behavior (e/e_0) from an initially saturated porous medium exhibits distinctly different stages often used for diagnostics and classification depending on the focus of the studies and the interpretation of the rate limiting processes—e.g., surface water content or transport within the soil [1]. Sherwood observed a "constant rate period" that was equal to the potential rate until the water content at the surface reached a critical value denoted as "critical water content" [3]. Then, the drying rate decreased. This "falling rate period" was separated into a period limited by the transport of vapor through a viscous air film at the surface and a period controlled by the transport of liquid and vapor through the porous medium to the surface. In an extensive review Van Brakel discusses various conditions affecting the behavior of drying curves, especially the period of constant drying rate (PCDR, denoted here as "stage 1") [1].

Notwithstanding Van Brakel's assertion that the PCDR does not really exist (and hence should be referred to as an "apparent" constant rate period), numerous experimental and theoretical studies have established the existence of such a constant phase during drying of porous media, typically under mild atmospheric demand. Part of the confusion stems from attempts to paint an overly simplified picture of the processes involved. For example, Philip distinguished between a "constant rate phase" that is governed by atmospheric conditions and a "falling rate phase" that is controlled by conditions within the porous media [4]. He subdivided the falling rate into a period independent of atmospheric conditions and heat flow and into a final period

sensitive to the heat flux. Similarly, Idso *et al.* distinguished three periods with a constant drying rate controlled by atmospheric conditions, a first falling period limited by transport of water to the surface, and a last period with very small water transport dominated by adsorption and evaporation of water from thin water films at the surface [5]. However, many of analyses overlook limitations to vapor exchange from partially wet surfaces to the atmospheric boundary layer above. These aspects were highlighted by Suzuki and Maeda [6] and Schlünder [7], showing that vapor flux through a viscous boundary layer is limited for a small ratio between the boundary layer thickness and size (or spacing) of wet patches at the surface. This added complexity may confuse the interpretation of drying behavior especially under high atmospheric demand with higher air flows as we will illustrate later. The coupling between the vapor transport through the viscous boundary layer and the water flow through the porous medium was analyzed numerically by Yiotis *et al.* [8]. They showed that the drying rate dropped when the liquid structures become too small to sustain mass transfer through the boundary layer.

Another classification of the drying stages was based on pore scale models. In a three-dimensional (3D) invasion percolation model Le Bray and Prat [9] and Yiotis *et al.* [10] related the stages of the drying processes to the liquid distribution within porous media. They characterized a first stage denoted as the "initial drying period" as initial air invasion into the system when the water content at the surface decreases. This is followed by a constant rate period associated with nearly constant water content at the surface and liquid flow from the interior to the surface through a continuous network of liquid-filled pores ("spanning liquid cluster evaporation regime"). In the falling rate period the evaporative demand is larger than the flow capacity through the continuous liquid network. Then, the drying rate is dominated by dissolution of liquid clusters close to the surface ("disconnected liquid cluster evaporation regime"). Finally, a "receding front period" with a dry surface and a receding front was distinguished ("receding front regime"). In this study, we elaborate on conditions required for sustaining stage-1 evaporation, focusing on the importance of the spanning liquid cluster evaporation regime.

B. Hydraulically connected transition zone ("film region")

Yiotis *et al.* [10] have shown numerically that a constant drying rate is maintained while liquid connections between the evaporating surface and drying front are maintained, and flow rates are sufficient to supply the evaporation rate at the surface. Thus, the width of the spanning liquid cluster [10] controls the duration of high evaporation rates associated with stage 1. We distinguish between the drying front width at the interface between completely liquid-filled pores and partially filled pores and the longer-range hydraulic connections that control flow from the front to the surface defined as the "film region" by Yiotis *et al.* [11], as shown in Fig. 1. The drying front width defined as the mean distance between the minimum and maximum positions of the interface was previously analyzed theoretically and experimentally [12,13]
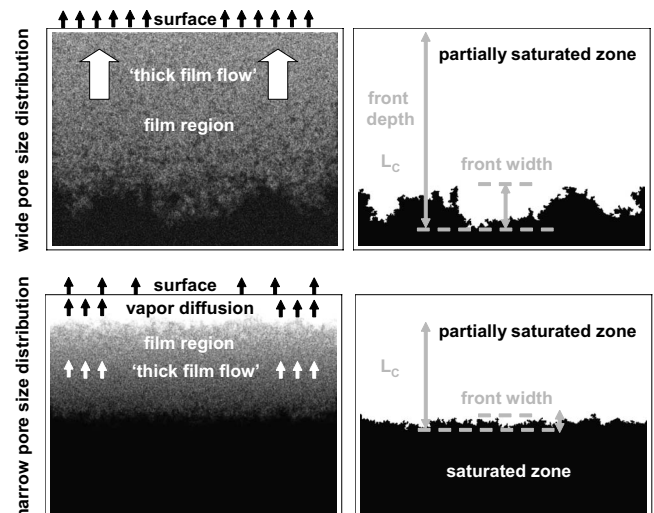

FIG. 1. Fluid distribution and flow regimes for evaporation from two porous media differing in pore size distribution computed with a three-dimensional invasion percolation model. The system consists of $400 \times 300 \times 50$ elements of size 0.1 mm with randomly distributed pore sizes. Completely water-saturated regions are shown in black, completely dry zones in white, and the region with thick liquid films in dark gray. For the wide pore size distribution the film region spans the entire zone from the drying front to the evaporating surface. Below, for the narrow pore size distribution, the film region is too short and an air-filled layer forms and limits liquid flow to the surface (vapor diffusion process). On the right side images are reclassified as water-saturated and partially saturated zones only. While the front width defines the roughness of the interface between these two zones, the characteristic length affects the maximum front depth at end of stage 1 of evaporation. For a narrow pore size distribution, both the characteristic length and front width are shorter.

and was shown to depend on both the mean pore size and width of the pore size distribution [14–18]. The impact of the pore size distribution was modeled with invasion percolation, and indeed the drying front width exhibits a dependence on the range of pore size (Fig. 1). Our emphasis in this study is on flow from the front to the surface along liquid-filled pores and not on the front width. These active "films" are comprised of liquid-filled crevices, pendular water at grain contacts and surface roughness, and are much thicker than films adsorbed by solid surface forces. Yiotis *et al.* [11] denoted the water retained in crevices as "thick films" and the adsorbed water as "thin films." Tuller and Or [19] used the terms "corner flow" and "film flow" to quantify the viscous resistances associated with these two liquid configurations in partially saturated media. Yiotis *et al.* [20] have shown that flow along liquid films to the surface enhances the drying rate compared to drying based on vapor diffusion through the pore space. Similarly, Eijkel *et al.* [21] measured an increase of the drying rate up to three orders of magnitude due to water flow in the corners of fractures.

C. Capillary-driven liquid flow

The spatial extent of the film region depends on capillary driving forces generated by water-filled fine pores at the sur-
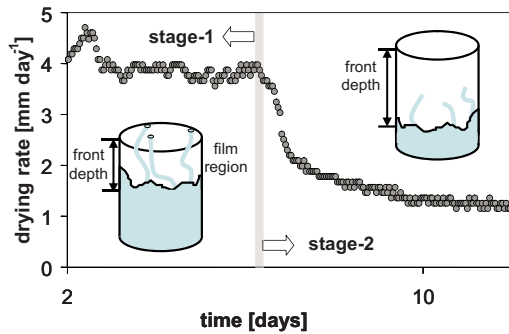
FIG. 2. (Color online) Conceptual diagram of first-stage evaporation. Drying rate measurements from sand with grain sizes ranging from 0.3 to 0.9 mm are shown. During the first stage, the drying rate is constant (potential drying rate $e_0 = 4$ mm day^{-1}). Water evaporates from the surface and liquid flows from the drying front to the surface within liquid-filled structures denoted as "thick films." At the end of stage 1, liquid connections break and the drying rate decreases (falling rate period). The drying front depth at the end of stage 1 is defined by the extent of the "film region" [11] and depends on the width of pore size distribution.

face, drying front depth, and viscous resistance to flow through liquid films. As the gas phase displaces preferentially liquid in large pores, liquid is retained in the smallest pores at the surface. As shown by Scherer [22], the capillary pressure difference between large pores at the drying front and fine pores at the surface induces liquid flow toward the surface. Such a flow process was termed "capillary pumping" by Yiotis *et al.* [23] or "funicular regime" by Coussot [24]. Typically, the capillary pressure gradient toward the surface is opposed by gravitational forces and viscous dissipation. Laurindo and Prat [13] and Prat and Bouleux [25] computed the lengths of liquid-filled regions needed to balance capillarity and gravity or capillarity and viscous dissipation based on the mean pore size of the medium. This interpretation is not compatible with the mechanistic description of Scherer [22] in which capillary forces are determined by differences in pore sizes and not by the mean pore size.

In this study, we extend this discussion and compute the spatial extent of the film region as a function of pore size distribution. The role of the width of the pore size distribution was previously analyzed with a capillary bundle model by Metzger and Tsotsas [26] where viscous dissipation balanced the capillary pressure difference between large and small capillaries (ignoring gravity). They found an increase in the period of the constant drying rate (stage 1) for media with a wider pore size distribution.

A general classification of drying stages and regions with different liquid phase distributions used in this study is shown in Fig. 2. In a first stage of the drying process the drying rate is not limited by liquid (and vapor) transport within the porous medium. The observed decrease in drying rates for high atmospheric demand is attributed to the limitation of vapor exchange with the overlying viscous boundary layer at the surface and not to water distribution within the porous medium; hence, we would classify the process as stage 1 as well. In many cases, the large and rapid drop in drying rates marking the end of stage 1 is attributed to abrupt

changes in liquid flow from a drying front to the surface due to breakage of liquid connections or vanishing capillary driving force.

This study focuses on the behavior during stage-1 drying of porous media as related to the existence of liquid films connecting the front with the surface. The specific objectives are to (i) demonstrate that the stage-1 duration and drying front depth at the end of stage 1 are controlled by an extended thick film region, (ii) quantify the maximum drying front depth at end of stage 1 using a characteristic length that can be deduced from the width of the medium pore size distribution, (iii) express the drying front characteristic lengths resulting from competition between capillarity, gravity, and viscous forces, and (iv) generalize the results by deducing the evaporation characteristic lengths and mass loss at end of stage 1 from parametric models for capillary pressure and liquid saturation (denoted as the water retention curve).

The paper is organized as follows: In Sec. II, the concept of evaporative characteristic lengths is introduced, followed by experimental procedures for determining drying rates and characteristic lengths in Sec. III. The results of the drying rates for two sands under different experimental conditions are presented in Sec. IV; these results and procedures are extended to general soils (based on published results) in Sec. V. A summary and conclusions are presented in Sec. VI.

II. THEORETICAL CONSIDERATIONS

We introduce a conceptual and parametric representation of characteristic lengths that control the transition from liquid-flow-supported stage 1 to diffusion-controlled stage 2 during evaporation from porous media. These characteristic lengths are expressed as equivalent distances between the evaporating surface and the drying front position at the end of stage 1. We identify a gravity-limiting length (L_G), the maximum vertical distance over which liquid-filled pores connect the drying front and the surface and sustain direct evaporation from the surface, and a viscous length (L_V) over which viscous dissipation becomes limiting (combining the effects of hydraulic conducting cross section and evaporation rate). As will be shown, these characteristic lengths are dependent on the width of the pore size distribution and on the relative importance of capillarity, gravity, and viscous forces. The origin and characteristics of these lengths will be illustrated for a pair of hydraulically interacting capillaries at the microscale and for a porous medium represented by its hydraulic functions at the macroscale.

A. Characteristic lengths for evaporation from a pair of capillaries

Consider a pair of capillaries that are hydraulically connected by a permeable interface [inset, Fig. 3(a)] [22]. The two capillaries are initially completely liquid saturated, and as liquid is lost by evaporation, capillary menisci with radius R form at the top, resulting in a capillary pressure drop p (or h expressed as head):
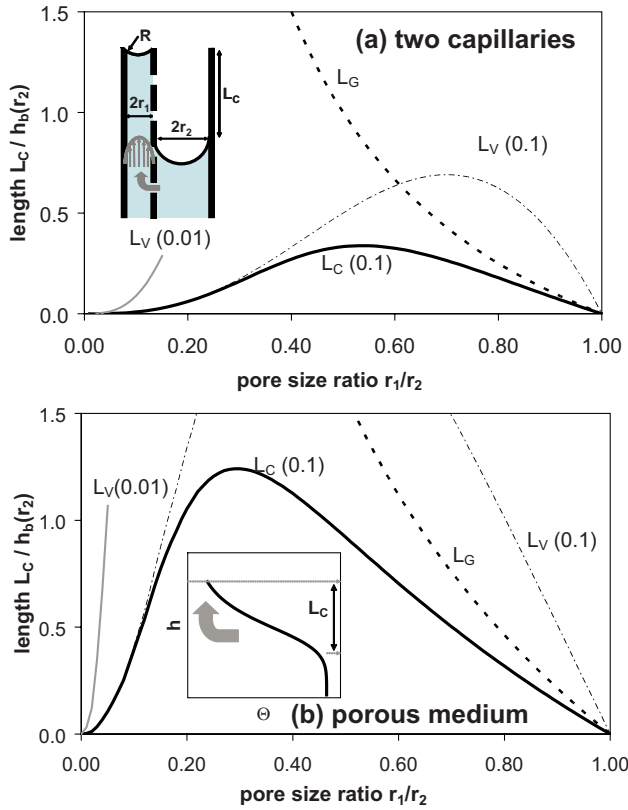
FIG. 3. (Color online) Effect of pore size distribution on the characteristic length L_C (end of stage 1) for (a) a pair of hydraulically connected capillaries and (b) a porous medium with hydraulic properties characterized by the Van Genuchten [27] and Mualem [28] models. Water flows from the drying front to the fine pores at the surface as indicated by the gray arrows. The characteristic length equals the maximum front depth and is a result of the interplay between capillarity, gravity, and viscous dissipation. Without the viscous effect (L_V), the characteristic length (L_C) would grow with decreasing size ratio due to increasing gravitation length (L_G). Due to viscous dissipation the lengths L_V and L_C depend on the evaporation rate that is indicated in parentheses as the ratio between the potential evaporation rate e_0 and the water-saturated hydraulic conductivity K_s. For the micro- and macroscopic cases the characteristic large pore has diameter $r_2 = 0.1$ mm and the lengths are divided by its air-entry value $h_b(r_2)$. For the macroscopic model, the small radius r_1 was determined as a capillary that drains for a capillary head of $h_b + \Delta h_{cap}$.

$$p = \frac{2\sigma}{R} \rightarrow h = \frac{2\sigma}{\rho g R}, \tag{1}$$

with g the acceleration due to gravity, σ the surface tension, and ρ the water density. The largest capillary pressure attainable within the large capillary with radius r_2 defines its air-entry value $h_b(r_2)$; hence, subsequent evaporation from the system would not change the meniscus curvature within the large capillary and a capillary pressure difference forms between the large and small capillaries which may attain a higher curvature ($1/R$). The capillary pressure difference Δp can also be expressed as head with the dimension of a length:

$$\Delta p = 2\sigma \left(\frac{1}{R} - \frac{1}{r_2} \right) \rightarrow \Delta h = \frac{2\sigma}{\rho g} \left(\frac{1}{R} - \frac{1}{r_2} \right). \tag{2}$$

Consequently, water flows from the large to the small capillary as the meniscus in the large capillary recedes. This capillary-driven mass flow in support of a certain evaporative demand at the surface may become limited by either gravitational or viscous forces as we see next.

1. Gravitational characteristic length

As evaporation progresses and the meniscus in the large capillary recedes, the distance to the evaporating surface increases, necessitating an adjustment in the curvature of the meniscus in the small capillary to accommodate the additional gravitational component until it reaches its intrinsic air entry value (the porous interface between the capillaries has much smaller pores than the fine capillary of radius r_1). Thus, the maximum capillary drive expressed in units of length for the two capillaries is given as

$$\Delta h_{cap} = \frac{2\sigma}{\rho g} \left(\frac{1}{r_1} - \frac{1}{r_2} \right). \tag{3}$$

This is the length at which the gravitational head difference Δh_G balances the maximum capillary driving force Δh_{cap} [22], causing cessation of flow, and could also be viewed as the characteristic gravity length $L_G = \Delta h_G = \Delta h_{cap}$ for the pair of vertical capillaries considered. Subsequently, the meniscus recedes into the smaller capillary and liquid evaporates from its interior and is transported to the surface by vapor diffusion. This change marks the end of stage-1 evaporation and the transition to slower and diffusion-limited stage 2. Note that the gravity length is independent of evaporation rate.

The relationship between gravitational and capillary forces can be expressed in terms of the Bond number Bo defined as

$$Bo = \frac{\rho g}{\sigma} r_2^2, \tag{4}$$

with r_2 chosen as the characteristic pore size. Expressing the small pore size as $r_1 = \gamma r_2$ with $\gamma < 1$, the gravity length L_G can be expressed as a function of Bo according to

$$L_G = \frac{r_2}{Bo} \left(\frac{2}{\gamma} - 2 \right). \tag{5}$$

This expression can be compared with the gravity length given in [13] and [25]. Here, the factor in parentheses reflects the effects of the pore size distribution width not considered in [13] and [25].

2. Viscous characteristic length

Liquid flow toward the evaporating top interface in the small capillary involves viscous dissipation where pressure head loss is proportional to flow velocity and to inverse capillary radius squared. The drying rate e_0 from the two (or more) capillaries with total cross-sectional area A is supplied by the flux density q flowing through the fine capillary (r_1):

$$e_0 A = q \pi r_1^2 \rightarrow q = e_0 \left(1 + \frac{r_2^2}{r_1^2}\right). \quad (6)$$

Evaporation from the meniscus in the small capillary is supplied by liquid flow according to the Hagen-Poiseuille equation

$$e_0 \left(1 + \frac{r_2^2}{r_1^2}\right) = q = \frac{r_1^2 \Delta p}{8 \eta L} = \frac{r_1^2 \rho g}{8 \eta} \frac{\Delta h_V}{L}, \quad (7)$$

with L the height difference between the large and small menisci, q the water flux density in the small capillary, η the dynamic viscosity, the factor of 8 for cylindrical capillary shape, and the pressure drop due to viscous dissipation Δp or Δh_V. We distinguish head loss due to viscous flow from the capillary head difference Δh_{cap} in Eq. (3) by the index V. Formally, Eq. (7) can be compared with the hydraulic conductivity K or permeability κ of a porous medium according to

$$K(\theta) = \frac{r_1^4 \rho g}{8 \eta (r_1^2 + r_2^2)} \rightarrow \kappa(\theta) = \frac{r_1^4}{8(r_1^2 + r_2^2)}, \quad (8a)$$

$$K_s = \frac{(r_1^4 + r_2^4) \rho g}{8 \eta (r_1^2 + r_2^2)} \rightarrow \kappa_s = \frac{(r_1^4 + r_2^4)}{8(r_1^2 + r_2^2)}, \quad (8b)$$

with the unsaturated hydraulic conductivity $K(\theta)$ and permeability $\kappa(\theta)$ as a function of water content θ with air in the large capillary r_2 and liquid in the small capillary r_1. For the saturated conductivity K_s and permeability κ_s both pores are water filled and contribute to liquid flow.

Rearranging Eq. (7) provides the head loss due to viscous dissipation as

$$\Delta h_V = \frac{8 L e_0 \eta (r_1^2 + r_2^2)}{\rho g r_1^4}. \quad (9)$$

To illustrate the viscous effect, it is instructive to neglect the influence of gravity (considering a horizontally oriented pair of capillaries); hence, the maximum distance between menisci, L_V, is attained when Δh_V due to viscous dissipation balances the capillary pressure head difference:

$$\Delta h_{cap} = \frac{2\sigma}{g\rho}\left(\frac{1}{r_1} - \frac{1}{r_2}\right) = \Delta h_V = \frac{8 L_v e_0 \eta (r_1^2 + r_2^2)}{\rho g r_1^4}$$

$$\rightarrow L_V = \frac{\rho g r_1^4}{8 e_0 \eta (r_1^2 + r_2^2)} \Delta h_{cap}. \quad (10)$$

L_V is the characteristic length for viscous dissipation (without gravity).

The ratio between viscous and capillary forces is expressed with the capillary number Ca defined for flow in porous media as

$$Ca = \frac{\eta e_0}{\sigma} \frac{r_2^2}{\kappa}. \quad (11)$$

Considering the viscous length in Eq. (10) and permeability in Eq. (8a) and (8b) the viscous length can be expressed as proportional to the capillary number:

$$L_V = \frac{r_2}{Ca}\left(\frac{2}{\gamma} - 2\right). \quad (12)$$

This expression differs slightly from the formulation given in [25] due to consideration of pore size distribution width and their definition of Ca without permeability.

3. Combined gravity and viscous lengths

Considering both gravity and viscous dissipation for evaporation from a vertical pair of capillaries the maximum combined head loss that must be overcome by capillary forces is

$$\Delta h_{cap} = \frac{2\sigma}{g\rho}\left(\frac{1}{r_1} - \frac{1}{r_2}\right) = \Delta h_V + \Delta h_G = \frac{8 L_C e_0 \eta (r_1^2 + r_2^2)}{\rho g r_1^4} + L_C, \quad (13)$$

with a distance L_C between the meniscus of the large pore and the surface that is equal to

$$L_C = \frac{\dfrac{2\sigma}{g\rho}\left(\dfrac{1}{r_1} - \dfrac{1}{r_2}\right)}{\dfrac{8 e_0 \eta (r_1^2 + r_2^2)}{\rho g r_1^4} + 1} \rightarrow L_C = \frac{L_G}{\dfrac{L_G}{L_V} + 1}. \quad (14)$$

For the right-hand expression, Eq. (10) and $L_G = \Delta h_{cap}$ were applied. As long as the gravitational length L_G is much shorter than the length defined by the viscous dissipation L_V, the combined length is equal to the gravitational length $L_C \approx L_G$.

Based on Eqs. (5) and (12) the denominator can be expressed as $Ca/Bo + 1$. As long as the capillary number Ca is small, the evaporation characteristic length is determined primarily by the capillary pressure difference.

To express the effect of the width of the pore size distribution (determined by r_2 and r_1) on the characteristic length, the maximum distance L_C between the surface and the meniscus in the large capillary is shown as a function of r_1/r_2 in Fig. 3(a). For a small ratio ($r_1 \ll r_2$) the capillary forces and the length L_G are high. However, for a small ratio r_1/r_2, the viscous flow through the fine capillary becomes limiting and the characteristic length L_C is shorter than the length determined by the interplay between capillary and gravitational forces alone. While the length L_G does not depend on the evaporation rate, L_V decreases with increasing e_0 due to the increased viscous losses. In Fig. 3(a), the characteristic lengths for viscous dissipation are shown for a drying rate $e_0/K_s = 0.1$ and 0.01.

The analysis presented in this section is easily extended to multiple hydraulically coupled capillaries or to a porous medium represented as a bundle of interacting capillaries [26].

B. Pore size distribution and characteristic lengths for evaporation from porous media

As with the conceptual model involving two interacting capillaries, air first enters the largest pores in a complex porous medium while menisci in smaller pores at the evaporating surface may remain in place (albeit with decreasing radii
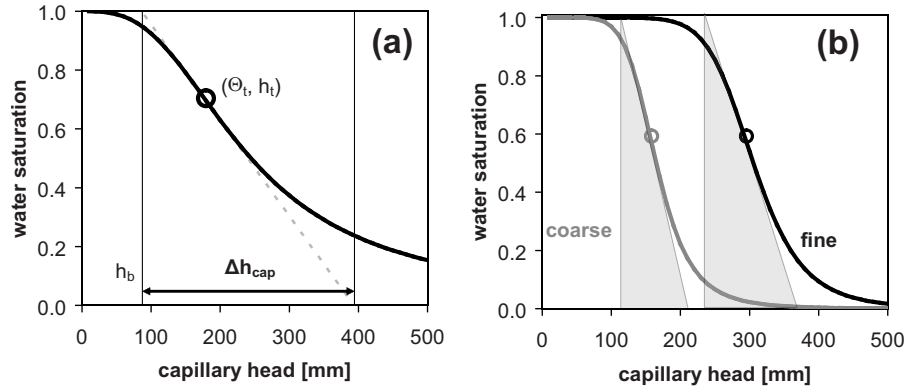
FIG. 4. Linearization of the water retention curve to determine the capillary pressure difference Δh_{cap}, which equals the gravitational length L_G. (a) To deduce the characteristic length from the water retention curve, the tangent at the (encircled) inflection point (Θ_t, h_t) is computed. The characteristic length is determined by the capillary head values of the tangent with saturation 1 and 0. (b) The curves fitted according to the Van Genuchten [27] model and the linear ranges indicated by the shaded triangle are shown for the two sand materials used in the experimental study.

of curvature). Thus, water flows from large pores with lower air-entry value to smaller water-filled pores toward the surface where evaporation occurs. Such mass flow may be sustainable as long as capillary driving forces are larger than gravitation and viscous forces.

1. Pore size distribution and gravity characteristic length

Experimental findings in sand (Sec. IV) maintain the idea that water-filled structures supporting mass flow from the drying front are spanned over a distance determined by the width of the pore size distribution. The width of the pore size distribution of porous media is often deduced from the relationship between capillary pressure and liquid saturation (denoted as the water retention curve). For equilibrium (hydrostatic) conditions, a water retention curve determines water saturation Θ as a function of height h above a water table. We propose that the difference between the capillary pressure required to invade or drain the largest pores (air-entry value) and the smallest drainable pores reflects the maximum range $\Delta h_{cap} = L_G$ for hydraulically connected water-filled pores. We distinguish between the smallest yet hydraulically connected pore structures supporting liquid flow and smaller structures with water transport along adsorbed water films or due to vapor diffusion and condensation. The maximum range for hydraulically connected water-filled pores can be deduced from the shape of the water retention curve. We used the Van Genuchten [27] parametric model for the water retention curve. The hydraulic functions according to the Van Genuchten [27] and Mualem [28] models are given below:

$$\Theta = \frac{\theta(h) - \theta_r}{\phi - \theta_r} = [1 + (\alpha h)^n]^{-(1-1/n)}, \qquad (15a)$$

$$K(\Theta) = K_s \Theta^\tau [1 - (1 - \Theta^{1/(1-1/n)})^{1-1/n}]^2, \qquad (15b)$$

with Θ the effective water saturation, $\theta(h)$ the volumetric water content for a pressure head h, θ_r the residual water content, ϕ the porosity that equals the water content for a completely water-saturated condition, α the inverse of a characteristic pressure head, and the parameter n attributed to

the pore size distribution. The unsaturated hydraulic conductivity $K(\Theta)$ contains an additional parameter τ related to the flow path geometry and connectivity and is generally set to 0.5. The pore size distribution parameter n decreases with increasing width of the pore size distribution. The Van Genuchten [27] model describes a small decrease in saturation for small capillary pressures (associated with air-entry pressure in the saturated medium), followed by a significant drop in saturation until the liquid phase disconnects and attains a residual water content value. Consequently, we consider capillary driving forces and water contents associated with the significant drop in saturation as the region with hydraulically connected thick liquid films.

To estimate the capillary pressure required for draining the largest and smallest drainable pores in this "active" range we linearized the water retention curve measured under hydrostatic conditions by determining the tangent at the inflection point. To compute the tangent, the first (equation of tangent) and second (inflection point) derivatives of Eq. (15a) were computed. The head value of the tangent intersecting with $\Theta = 1$ defines the air-entry value h_b, and the pressure $h_b + \Delta h_{cap}$ is determined by the intersection of the tangent with $\Theta = 0$. This procedure is shown and applied in Fig. 4. Due to the equivalence between head and the height above a free water level, the head difference Δh_{cap} equals L_G. The resulting gravity characteristic length is

$$\Delta h_{cap} = L_G = \frac{1}{\alpha(n-1)} \left(\frac{2n-1}{n} \right)^{(2n-1)/n} \left(\frac{n-1}{n} \right)^{(1-n)/n}, \qquad (16)$$

and the air-entry value h_b is

$$h_b = \frac{1}{\alpha} \left(\frac{n-1}{n} \right)^{(1-2n)/n} - \Delta h_{cap}. \qquad (17)$$

A linearization of the Brooks-Corey [29] model of the water retention curve with a parameter λ attributed to the pore size distribution was tested as well and showed similar properties. Alternatively, the range of hydraulically connected pores

could be deduced from measured values $\theta(h)$ by computing $\Delta\theta/\Delta h$. This approach will be applied in an example in Sec. V.

2. Pore size distribution effects on the viscous characteristic length

When viscous effects can be neglected, water flow from the receding drying front to an evaporating surface above is sustained as long as the distance between the front and the surface is smaller than the gravitational length L_G. To evaluate the role of viscous dissipation during evaporation for a drying front at depth L, we express the water flow supporting evaporation rate e_0 with a Buckingham-Darcy law for unsaturated flow as

$$e_0 = q = K(\theta)\frac{\Delta h_V}{L} \rightarrow \Delta h_V = \frac{Le_0}{K(\theta)}, \qquad (18)$$

with the head difference Δh_V and the unsaturated hydraulic conductivity $K(\theta)$. For simplicity, we first consider horizontal flow without gravity. Balancing the capillary driving force and viscous dissipation we find the maximum distance between the drying front and evaporating surface in the absence of gravity as

$$\Delta h_{cap} = \Delta h_V = \frac{L_V e_0}{K(\theta)} \rightarrow L_V = \frac{K(\theta)}{e_0}\Delta h_{cap}. \qquad (19)$$

3. Combined gravity and viscous lengths

When considering both viscous dissipation and gravity forces, the maximum drying front depth for the end of stage-1 evaporation is estimated from

$$\Delta h_{cap} = \Delta h_V + \Delta h_G = L_C\left(\frac{e_0}{K(\theta)} + 1\right) \rightarrow L_C = \frac{L_G}{1 + \dfrac{e_0}{K(\theta)}}. \qquad (20)$$

For small values of the ratio of the potential evaporation rate to unsaturated hydraulic conductivity $[e_0/K(\theta)]$, $L_C \approx L_G$. As in Eq. (14) the effective characteristic length in Eq. (20) can be expressed as a function of gravitational and viscous lengths by inserting Eq. (19) and $L_G = \Delta h_{cap}$.

The determination of the characteristic length for the end of stage 1 requires estimates of the unsaturated hydraulic conductivity $K(\theta)$ and water content distribution above the drying front. These estimates were obtained based on three simplifying assumptions: (i) the water content distribution above the drying front can be deduced from the (hydrostatic) water retention curve and (ii) the water content above the front decreases linearly from saturation at the drying front (with pressure h_b) to the residual water content θ_r at a distance L_C from the front. The linear relationship was shown to be a good approximation for sand media analyzed in our experiments (Secs. III and IV). Additionally, Shimojima *et al.* [30] reported a linear water content profile close to the hydrostatic boundary conditions above the drying front. However, a linear water content profile is not essential for

the analysis and any functional form between water content and head can be used. Based on the linear profile we estimate the remaining water above the front according to $\frac{1}{2}(\phi - \theta_r)L_C$. The third simplifying assumption relates to changes in the hydraulic conductivity: (iii) we assume that the unsaturated hydraulic conductivity varies from $K(h_b)$ at the front to $K(h_b + \Delta h_{cap})$ at the surface and use its mean value as a first approximation to estimate the viscous resistance to flow. The mean hydraulic conductivity parametrized according to the Van Genuchten [27] and Mualem [28] models for a hydrostatic water content distribution above the drying front was estimated as

$$\overline{K(h)} = \frac{1}{\Delta h_{cap}}\int_{h=h_b}^{h=h_b+\Delta h_{cap}} K_s[1 + (\alpha h)^n]^{-(1-1/n)\tau}$$

$$\times\left[-1 + \left(1 - \frac{1}{1 + (\alpha h)^n}\right)^{1-1/n}\right]^2 dh. \qquad (21)$$

Note that to express the hydraulic conductivity as a function of pressure head, we inserted Eq. (15a) into (15b).

The characteristic lengths according to Eqs. (19) and (20) are shown in Fig. 3(b) as a function of the width of the pore size distribution. To compare the macroscale analysis with the two capillaries (microscale) of size r_2 and r_1, we express two characteristic pores sizes using the capillary law:

$$r_2 = \frac{2\sigma}{\rho g}\alpha, \qquad (22a)$$

$$r_1 = \frac{2\sigma}{\rho g(h_b + \Delta h_{cap})}, \qquad (22b)$$

$$\frac{r_1}{r_2} = \frac{1}{\alpha(h_b + \Delta h_{cap})}, \qquad (22c)$$

with α the inverse of a characteristic head in the Van Genuchten model of the water retention curve [27]. As in the case of the microscopic analysis, the characteristic length increases for decreasing ratio r_1/r_2 until the viscous dissipation becomes limiting. This figure reveals that the width of the pore size distribution has a dominant influence on the characteristic length and therefore on the evaporation rate. Obviously, the characteristic lengths are not equal for media with the same mean or maximum pore size, but are dominated by the width of the pore size distribution. For uniform pore sizes ($r_1/r_2 = 1$) the characteristic length equals 0 and no stage 1 is expected.

III. EXPERIMENTAL CONSIDERATIONS

A. Sand media and their hydraulic properties

Two quartz sand media with particle sizes ranging from 0.1 to 0.5 mm (denoted as "fine sand") and from 0.3 to 0.9 mm ("coarse sand") were used in a series of evaporation experiments as described below. The same sands were used in other studies [31], and the hydraulic properties are well characterized. Additionally, the pore structures of these sand media were measured and quantified using synchrotron ra-

diation, and this information enables a comparison of the evaporation behavior with the geometrical properties of the pore space. The water retention curve of the scanned material was computed using a morphological pore-network model [32]. Based on insertion of discrete spheres of progressively larger sizes into the imaged pore space, the pore size of each element of the pore space was determined. Based on an invasion-percolation algorithm, the invasion of air was computed as a function of the pore size and the connectivity of the pore space.

Although the hydraulic functions were measured for the same sand material in a previous study [31], the packing procedure (see next subsection) in our case was slightly different to ensure a completely water-filled pore space. We thus repeated some measurements of the hydraulic functions in our laboratory. The water retention function was determined by the *hanging column* method [33] using samples with diameter of 52 mm and height of 50 mm packed with the sands and placed on a porous plate with an air-entry value of about 600 mm (corresponding to a pressure of 5.89 kPa or to an equivalent pore with a diameter of 0.05 mm at air entry). The bottom of the sample was connected to a movable water reservoir that controls the applied pressure with the height difference between the reservoir and the porous plate. The height difference corresponds to the force exerted by the height of a hanging column that drains the sample. The top of the column was covered with foil to reduce evaporation with a few holes to maintain atmospheric pressure at the top. The suction head was varied at 30-mm intervals for the coarse sand and 50-mm intervals for the fine sand. The columns were mounted on a balance and the mass was monitored to determine the water mass within the column when the equilibrium for the applied pressure value was reached. For various positions of the water level corresponding to a pressure head at the bottom of the column, the remaining water mass within the column was determined.

For the saturated hydraulic conductivity, we applied the *falling-head* method [33] using a 100-mm-long water-saturated sand column (50 mm diameter) connected to cylindrical water reservoir (100 mm in diameter with a 20-mm-diameter tube). The hydraulic conductivity is deduced from the changes in water level in the reservoir with time recording both the volume of flow and driving pressure. The large dimensions of the tube and the reservoir were chosen to minimize flow resistance.

B. Evaporation studies

Experiments were conducted to quantify the evaporation rates from sand-filled cylindrical Plexiglas columns (diameter of 54 mm and length of 50–350 mm) and rectangular Hele-Shaw cells (260 mm in length, 10 mm in thickness, and 75 mm in width) with top boundary open to the atmosphere. The columns were placed on digital balances to automatically determine drying rates from mass loss at intervals between 0.5 and 5 min. The potential evaporation rate for the experimental conditions was determined from concurrent measurements of evaporation from a water-filled column subjected to similar conditions (the water surface was main-
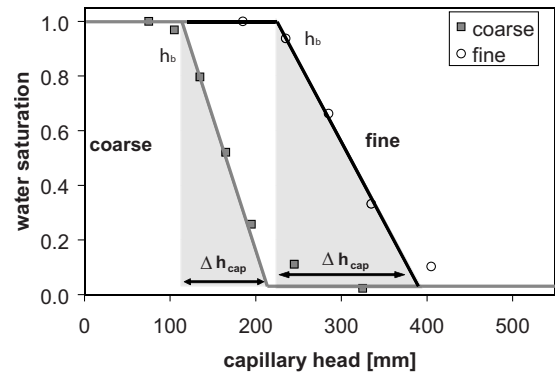

FIG. 5. Linear range of the water retention curve based on linearization of measured values of mean water saturation in a column of 50 mm in length for various pressure steps. The width Δh_{cap} of the linear range corresponds to a maximum span of liquid films connecting the drying front and evaporating surface (when viscous dissipation is negligible).

tained constant using a *Mariotte bottle*). Additionally, air temperature and humidity were measured using a computer-controlled sensor (Hygrowin, rotronic, Switzerland). In some experiments we used a hair drier to control air flow above the columns and manipulate potential drying rates.

Initially, the columns were completely water saturated using degassed water and flushing sand particles with degassed water before the columns were packed. Sand particles were deposited directly into the water-filled columns, keeping the liquid level a few centimeters above the sand surface. Such a packing procedure may result in size segregation and higher porosity than dry packing. To circumvent this problem, we first added about 40 g of wet sand to the column and then mixed the first 1–2 cm to rearrange the particles, resulting in a higher density. Despite the risk of introducing a certain degree of heterogeneity, the complete removal of air bubbles and resulting constant porosity (in the range of 0.40–0.42) were critical for quantification of the evaporation behavior.

In some experiments, a degassed dye solution (brilliant blue, $0.5-1.0$ g l^{-1}) was used to enhance the visibility of the fluid distribution and for automatic imaging. In one experiment we analyzed the R (red), G (green), and B (blue) values of the color image to delineate the dynamics of the front. The color values were integers ranging from 0 to 255. We used the ratio $g=(1+G)/(1+B)$ as the gray value for further analysis. First, the filtered gray-valued image was segmented into pixels of the liquid-saturated and partially air-filled zone based on the frequency distribution of the gray values. The pixel of the interface between the water-saturated and the unsaturated zones with the highest distance from the surface was chosen as front depth.

IV. RESULTS

A. Hydraulic properties of sand media

The measured saturated hydraulic conductivity was 58.8 m day^{-1} for the fine sand and 225.1 m day^{-1} for the coarse sand, and for both media, was considerably higher than the evaporation rates of a few mm per day. We linear-

ized the water retention curve as shown in Fig. 5 for capillary head values in the range of 120–210 mm for coarse sand and 230–370 mm for the fine sand. Additionally, we fitted the Van Genuchten [27] model to the data, obtaining estimates of air-entry values of 117 and 236 mm and the capillary width of a linear range of 96 and 138 mm for the coarse and fine sands, respectively. These results confirm estimates of the driving capillary pressure head difference Δh_{cap} (or gravity-limited length L_G) of 90 mm for coarse sand and 140 mm for fine sand.

To relate this estimate of the gravity-limited length L_G to the spatial distribution of the liquid phase and its connectivity, we analyzed the water configuration in images of the pore structure obtained using synchrotron x-ray data [32]. The water and air distribution for an image with 600^3 nodes consisting of elements (denoted as voxels) of size 0.011 mm was computed for increasing pressure applied at the bottom. Quantifying pore sizes using discrete sphere sizes [32] supported the application of only a limited number of pressure steps. The distribution of solid particles and fluid phases for different pressures is shown in Fig. 6. Initially, air enters the large cavities within the pore space and water remains in contacts and crevices. With increasing pressure, air invades the spaces between sand grains and the liquid phase becomes more fragmented. In the cross sections shown in Fig. 6, we distinguish between water that forms a continuous three-dimensional structure spanning top and bottom of the image and water belonging to disconnected clusters. The analysis of phase connectivity was carried out in a center cube with 400^3 nodes to limit the effects of the boundary. The distributions depicted in Fig. 6 correspond to pressure head values of 385 mm for fine sand and 245 mm for coarse sand. These values exceed the linearized range of the water retention curves, $h_b + \Delta h_{cap}$ (370 mm for fine sand and 210 mm for coarse sand), at which liquid becomes disconnected and hydraulic continuity is disrupted. These morphological changes, which correspond to breaking of "thick films" between the drying front and surface, are expected to induce changes from stage 1 to stage 2 in the drying behavior.

B. Determination of the drying front depth

An evaporation experiment from Hele-Shaw cells (260 $\times 75 \times 10$ mm) focused on tracking the evolution of the drying front in coarse and fine sands. The two media were placed side by side, separated by an impervious glass barrier. The images of dye distributions were classified as "wet" and "partially air-filled" regions as described in Sec. III. The minimum position of the drying front as a function of time is shown in Fig. 7. During the first phase (stage 1), the depth of the drying front increases linearly with time until the front reached depths of 90 mm for the coarse sand and 140 mm for the fine sand. These depths correspond to the pore size width (capillary drive) estimated from linearization of capillary pressure water saturation relationships as shown in Fig. 5 and discussed in the previous subsection. As the drying front receded deeper into the respective medium and exceeded the gravity characteristic length L_G, a drop in the observed drying rate ensued (as seen in the slope of the front depth with
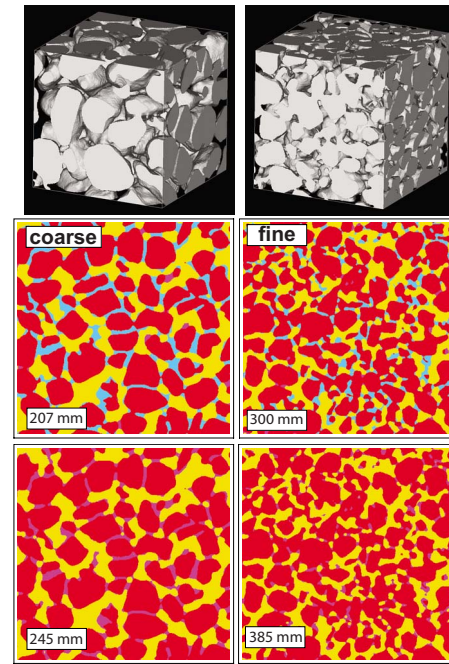

FIG. 6. (Color online) Simulated front displacement using a morphological pore network model [32] to visualize formation and connectivity of "thick films." The sand samples (15 mm in diameter) were analyzed using synchrotron x-ray tomography at a spatial resolution of 0.011 mm to describe the pore spaces. The arrangement of sand grains for fine and coarse samples is shown for cubes with 200^3 voxels (a voxel is the unit of a three-dimensional image). The fluid distribution was computed for a larger image with 600^3 voxels. Horizontal cross sections with 400^2 pixels from the center of the sample at two different values of suction are shown with solids in red, air in yellow, continuous water in blue, and disconnected water in dark pink. The connectivity refers to the three-dimensional arrangement of the water phase and cannot be deduced from cross sections alone. The highest applied suction value was chosen to exceed the linear range of the water retention curve for each sand ($h_b + \Delta h_{cap} = 210$ mm for coarse sand and 370 mm for fine sand). Liquid remaining in crevices and grain contacts become disconnected, resulting in cessation of flow.

time). These changes are attributed to a disruption of hydraulic connectivity and subsequent transition to water transport by means of vapor diffusion. A larger characteristic length for the fine sand results in more water loss as compared with coarse sand during stage 1. A separation in drying front penetration rates for the two sands coincides with a transitioning of coarse sand to vapor-diffusion-controlled stage-2 evaporation.

C. What determines the duration of stage-1 evaporation?

The diagnostic information contained in drying front dynamics is useful for delineating characteristic lengths and for detecting differences in drying rates between fine- and coarse-textured sands. However, the drying rates and evaporated mass cannot be accurately deduced from such geometrical information. To assess actual water loss, the water content above the drying front must also be known. We de-
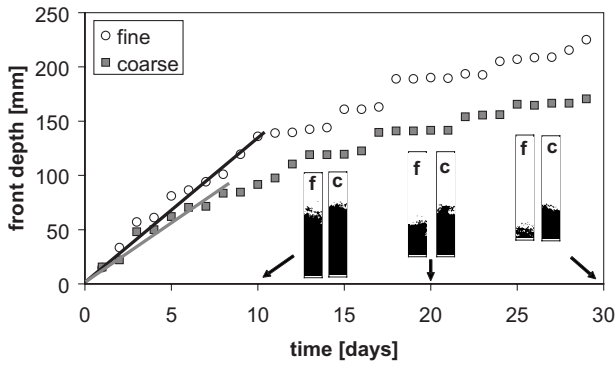
FIG. 7. Dynamics of the drying front depth in coarse and fine sand as a function of elapsed time measured in Hele-Shaw cells of 26 cm in length. For each time step, the minimum position of the drying front was determined by image analysis. With increasing time, the drying front recedes deeper into the fine sand. For a constant evaporation rate (stage 1, indicated by lines) the front depth increases linearly with time to a depth of about 90 mm for the coarse sand and 140 mm for the fine sand. For 10, 20, and 30 days after the start of the experiment the corresponding liquid-saturated (black) and partially air-filled (white) zones are shown for the coarse (c) and fine (f) sands.
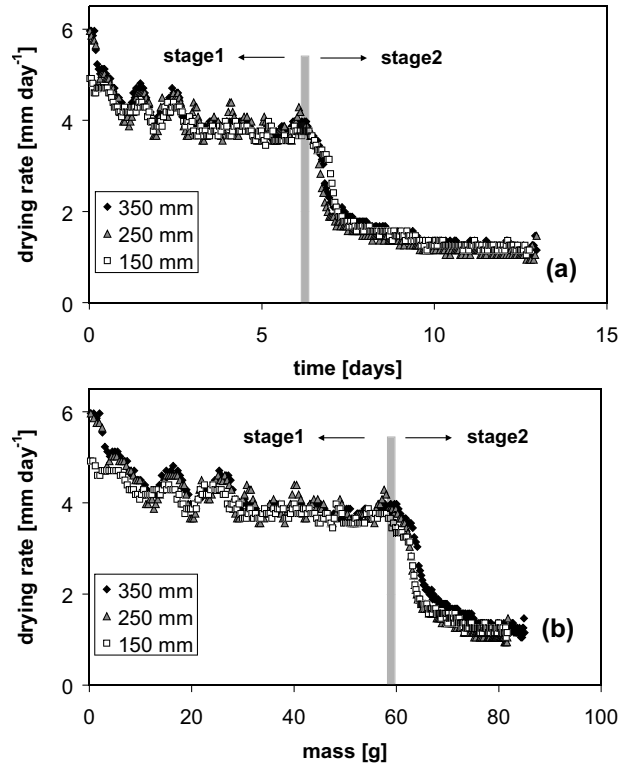

FIG. 8. Evaporation from coarse sand (0.3–0.9 mm) columns. The drying rate is given as a function of (a) time and (b) cumulative evaporated mass. For columns with length ranging from 150 to 350 mm, the drying rate dropped after a mass loss of 60 g. For a water content distribution based on the water retention curve only 41 g would drain out. During a drying process, additional water is lost, probably due to evaporation inside the porous medium.

termined drying rates in a series of experiments by directly measuring the mass loss as a function of time. Evaporation rates for atmospheric conditions with 28 °C temperature and 38% relative humidity from three columns filled with coarse sand with diameter of 54 mm and lengths 150, 250, and 350 mm are depicted in Fig. 8. In all columns, the drying rates were initially nearly constant at about 4 mm day^{-1} followed by a notable drop after an elapsed drying period of 6 days and a corresponding mass loss of 60 g. It is interesting to note that in a similar experiment using a short column (50 mm) the evaporation rate dropped abruptly after a 40-g mass loss (the total water mass in the column was 45 g). Clearly, this behavior reflects limited column length rather than porous medium properties; it also suggests that deducing the duration of the constant drying rate using samples shorter than the capillary or gravitational characteristic length is inappropriate (implications will be discussed in Sec. V).

Experiments compared drying rates from fine and coarse sands with potential drying rates ranging from 2 to 9 mm day^{-1}. As expected, the highest initial evaporation rate corresponds to high temperature and low humidity (28 °C and 31% humidity), whereas the lowest evaporation occurred for cool and humid conditions (21 °C and 58% humidity). To facilitate a comparison of the results from different cross sections, the evaporated water volume was divided by a sample cross section, yielding the evaporation depth. The results shown in Fig. 9 indicate that the evaporation rate in coarse sand dropped after a mass loss equivalent to 27 mm of water, and for fine sand, the drop in evaporation rate occurred after a 48.5-mm equivalent water depth. The ratio between evaporated water depths at the end of stage 1 (27 and 48.5 mm) for coarse and fine sand was similar to the ratio of their respective characteristic lengths (90 and 140 mm). Based on the assumption of a linear decrease of water content between the drying front and the surface (e.g., shape

of the water retention curves), we estimate the evaporation depth at the end of stage 1 as $\sim \frac{1}{2}(\phi - \theta_r)L_G$ corresponding to 18 mm (coarse) and 28 mm (fine). The difference between the measured and estimated water content profiles indicates an enhanced mass loss during evaporative drying compared with the expected profile for the drainage process. The additional mass loss might be attributed to internal losses by vapor diffusion and complete drying near the surface.

For experiments with initial drying rates of more than 4 −6 mm day^{-1}, the drying rate during stage 1 was not strictly constant, but decreased with time. Often such a decrease in drying rate is attributed to a limiting water supply due to diminishing hydraulic conductivity; however, this is not the case for the sands used here. Notwithstanding a decrease in hydraulic conductivity with distance from the receding drying front in sand, water flow is expected to remain sufficiently high at least in the beginning of the drying process. However, the observed drying rate began to decrease immediately after the onset of the process [Fig. 9(a)] and this decrease cannot be attributed to the hydraulic conductivity (the near-surface water content is high, supporting a large conductivity). It is instructive to assess the limitation of hydraulic conductivity by comparing values of the unsaturated hydraulic conductivity with evaporative flux when the hydraulic gradient is 1.0. Based on the hydraulic parameters [31] for a column with lower initial water content (0.32 and
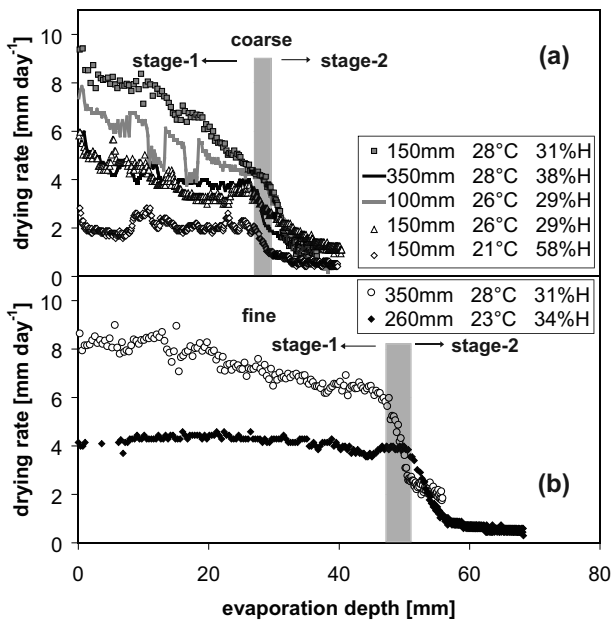
FIG. 9. Measured drying rates for various columns filled with coarse sand (a) and fine sand (b). In the legend the length of the column, the temperature, and the humidity are given. To compare the results obtained with columns of different cross section and shape, the evaporated mass loss is divided by the cross section of the media. For the coarse sand, the first drying stage period ends after a loss of 26–28 mm. For the fine sand, it is between 47 and 50 mm. The ratio between the two heights is similar to the ratio of the widths of the pore size distributions.

0.33 m^3 m^{-3} for coarse and fine sand), considering estimates of the saturated hydraulic conductivity (48 and 13 m day^{-1}), the average water content above the front must decrease to 0.03–0.04 m^3 m^{-3} before the hydraulic conductivity becomes limiting for a drying rate of 10 mm day^{-1}. Considering the considerably higher water content values above the drying front measured during this study, we conclude that the hydraulic conductivity was not limiting.

This leads to the hypothesis that vapor exchange between the partially dry surface and the viscous boundary layer above is limiting for high potential drying rates. Higher drying rates were induced by increasing air flow velocity over the columns (using a hair drier). Interactions between patchy surface wetness and the viscous boundary layer affect vapor exchange; these may be lumped into a mass exchange coefficient [6,7] or expressed as a resistance term [34]. The key characteristics affecting vapor flux from the partially wet surface to an air stream above include the vapor concentration gradient at the surface, the thickness of the boundary layer, partial surface wetting, and details of liquid arrangement on the drying surface [6,7]. Suzuki and Maeda [6] and Schlünder [7] have shown that the mass exchange coefficient is critically dependent on the ratio of the boundary layer thickness and patchiness of the partially wetted surface. While the absolute drying rate from porous media is expected to increase with decreasing boundary thickness (due to enhanced convection and surface vapor pressure gradient), its value relative to evaporation from free water surface decreases [6,7]. A more detailed and quantitative analysis of the

process is beyond the scope of this study and is left to future work. We conclude that the observed decreasing drying rates for initially saturated sand results from limited vapor transport through the viscous boundary layer and is not limited by medium transport properties. Because the drying front dynamics and internal transport processes remain the same as in a constant drying period (for low evaporation rates), we classify the evaporation period limited by boundary layer resistance as stage 1 as well.

Viscous losses expressed by the viscous characteristic length L_V [Eq. (19)] may also affect the duration of stage-1 evaporation. No direct measurements of water unsaturated hydraulic conductivity were made; hence, we can only estimate the role of viscous losses in our experiments. For standard parametrization of hydraulic functions [27,28], the unsaturated hydraulic conductivity at the surface corresponding to capillary head values of 210 mm (coarse) and 370 mm (fine) at end of stage 1 is 1182 and 331 mm day^{-1} for coarse and fine sand, respectively. Considering a drying rate of 4 mm day^{-1}, the corresponding head losses are 0.3 and 1.7 mm [Eq. (18)] for coarse and fine sand, respectively. The corresponding viscous lengths for coarse and fine sand of 26 600 mm and 11 600 mm [Eq. (19)] are considerably higher than the gravity lengths of 90 and 140 mm, and hence would not be limiting for these conditions. The role of viscous dissipation would undoubtedly become important for evaporation from fine-textured media at which the viscous length could become limiting before the gravitational length [35].

In two experiments, the distribution of the dye and water loss was measured concurrently. For the experiment with a potential evaporation rate of about 6 mm day^{-1}, the fluid distribution at the end of stage 1 is shown in Fig. 10. The position of the front is close to the characteristic length $L_C \approx L_G$, which corresponds to the width of the pore size distribution Δh_{cap} that was determined by linearization (Fig. 5). As soon as the drying front depth exceeds this length, liquid connections between the surface and the drying front break and evaporation proceeds via vapor transport at a reduced evaporation rate. This result is corroborated by data from another experiment with a potential rate of 2 mm day^{-1}.

V. EVIDENCE FOR THE ROLE OF PORE SIZE DISTRIBUTION IN EVAPORATION

In previous sections we have shown that the width of the pore size distribution determines the extent of the capillary driving force that determines the (hydraulically connected) characteristic length for the drying front depth at the end of stage 1. The following section attempts to generalize these findings based on different porous media reported in the literature. We first compare the predictions of mass loss during stage 1 based on the characteristic length using a numerical flow simulation based on the Richards equation similar to the study of Kozak *et al.* [36]. We then present comparisons with various evaporation experiments, focusing on stage-1 characteristics reported in the literature.

A. Comparison with numerical analysis based on the Richards equation

Kozak *et al.* [36] analyzed the effect of soil textural class (pore size distribution) on cumulative mass loss during the
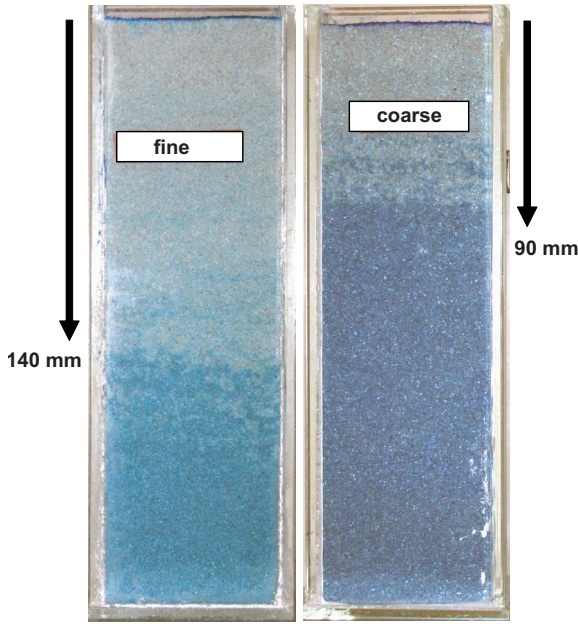
FIG. 10. (Color online) Dye distribution at the end of stage 1. The potential evaporation rate was 6 mm day^{-1} for the two Hele-Shaw cells. The arrows denote the extension of the gravitational length L_G deduced from the linear range of the relationship between capillary pressure and water saturation. This characteristic length is close to the observed depth of the drying front between the stained water-saturated region and the partially air-filled region.

stage-1 evaporation rate. They evaluated evaporation from 11 textural classes based on a numerical solution of the Richards equation [37]. The Richards equation combines mass conservation and water flow according to the Buckingham-Darcy law expressed for one-dimensional flow as

$$\frac{\partial \theta}{\partial t} = \frac{\partial \theta}{\partial z}\left[K(h)\left(\frac{\partial h}{\partial z} + 1 \right) \right], \tag{23}$$

with time t and soil depth z. Kozak *et al.* [36] computed the drainage process for different potential drying rates e_0 and defined a surface water potential value of 15 bars as a criterion for the end of stage 1. The soil columns were of 3 m in length with an initial saturation of 90%. To parametrize the hydraulic functions for different soil classes they used the Brooks-Corey [29] model parameters determined by Rawls *et al.* [38] for the 11 soil classes. In contrast to the laboratory experiments presented in Secs. III and IV, they allowed free drainage at the lower boundary. To enable a comparison between the characteristic length and numerical results for various soil classes, we repeated the numerical experiments for a system with a no-flux lower boundary condition. The Richards equation was solved using the HYDRUS 1D model developed by Simunek *et al.* [39]. The soil hydraulic functions were parametrized according to the models of Van Genuchten [27] and Mualem [28], and the parameters for the different soil classes chosen as published in Carsel and Parrish [40]. The initial condition was set to be a constant capillary head with depth of −1 mm. The choice of this initial pressure condition (corresponding to complete saturation) cir-

cumvents the internal drainage that would be observed for an initial water saturation of 90%. Mass loss during stage 1 was simulated for potential drying rates $e_0 = 3.0$ and 10 mm day^{-1} from a 3-m-long soil-filled column.

To analyze the stage 1 based on the characteristic lengths as a function of e_0 and the pore size distribution index n, we fitted the characteristic head $1/\alpha$ and the water-saturated hydraulic conductivity K_s given in [40] as a function of n for the textural soil classes according to

$$\alpha = 0.0087(n-1) \quad [\text{mm}^{-1}], \tag{24a}$$

$$K_s = 0.0077\, n^{7.35} \quad [\text{m day}^{-1}], \tag{24b}$$

with correlation coefficients (R^2) of 0.94 and 0.92, respectively. These functions can be used to estimate L_C for $e_0 = 3$ and 10 mm per day based on Eqs. (20) and (21).

To compare mass loss with the characteristic length (equal to the front depth at end of stage 1) the mass loss (or evaporation depth) must be expressed as front depth. For that purpose, we assume a linear decrease of the initial water content from θ_i at the drying front to θ_r at the surface. First, we divide the evaporation depth with the initially water filled cross section (θ_i-θ_r) and obtain a depth d. Then, for the linearized water retention curve d equals $\frac{1}{2}L$ with front depth L. For the numerical experiments and the laboratory experiments presented in Sec. IV the initial water content θ_i equals the porosity ϕ. For other experiments (presented in the next subsection) the initial water content value may be smaller and the initial capillary pressure is more negative than the air-entry value h_b at the emerging front. Due to the reduced initial water content, the amount of water evaporated in stage 1 is less than for completely water-saturated initial conditions and the front depth L at the end of stage 1 will be at a depth $(\theta_i - \theta_r)/(\phi - \theta_r)\,L_C$. Based on this consideration, the front depth L_C corresponding to completely water-saturated initial conditions can be deduced from the initial water content $\theta_i < \phi$.

In Fig. 11, the front depths at the end of stage 1 based on the Richards equation are compared with the characteristic length formulated in Eqs. (20) and (21) and using the relationship given in Eq. (24a) and (24b). For both approaches, based on the Richards equation and using the characteristic length, the front depth first increases with decreasing n due to the dominance of the gravitational length and then decreases for $n < 1.5$ due to the limiting viscous dissipation. Both approaches compute a higher mass loss and front depth for the smaller potential drying rate. The most pronounced difference between the numerical simulations and the characteristic length was found for coarse-textured media ($n > 2$). For coarse-textured media the stage 1 is dominated by the gravity length L_G and viscous dissipation is less important. Based on the concept of the characteristic length we hypothesize that the hydraulic connections to the surface may break due to the enhanced gravitational forces and the water supply along the thick films stops. This abrupt change in hydraulic connections is not described by the Richards equation and the water supply is also simulated for capillary head values at the surface that are larger than $h_b + \Delta h_{\text{cap}}$. For that reason, the front depth values based on the Richards
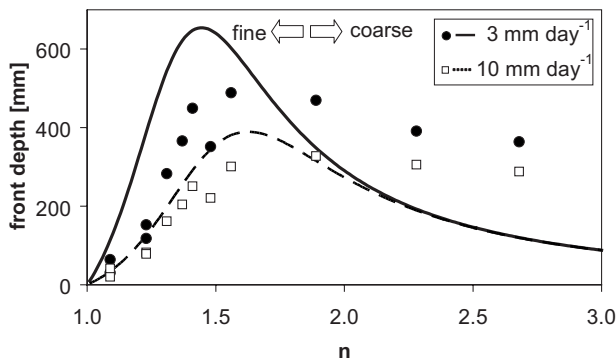
FIG. 11. Effect of pore size distribution parameter n on mass loss during stage 1 deduced from characteristic length L_C (lines) and compared with numerical simulations (symbols) based on solution of the Richards equation. For estimation of the characteristic lengths, the relationship $K_s(n)$ and $\alpha(n)$ for the saturated hydraulic conductivity K_s and the characteristic head $1/\alpha$ given in Eq. (24a) and (24b) were used. The evaporation depth obtained in the numerical studies is expressed as the drying front depth at the end of stage 1.
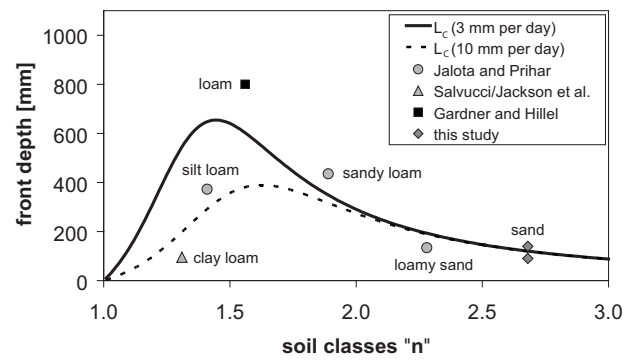

FIG. 12. Comparison between characteristic length as a function of textural classes and measured mass loss at the end of stage-1 evaporation. The measured evaporation depths are expressed as the drying front depth at the end of stage 1. The measured results were attributed to the pore size distribution values n that are typical for the corresponding textural classes [40]. Gardner and Hillel [45] and Jalota and Prihar [42] used columns of 1250 mm and 950 mm in length, respectively, and Jackson et al. [43] measured the evaporation from lysimeters (analyzed by Salvucci [44]).

equation are higher than the characteristic lengths for coarse-textured porous media.

B. Comparison with stage-1 evaporation data from the literature

Inspection of the experimental results from a range of soil textures that could have been useful for testing concepts outlined in this study, unfortunately, show that many drying experiments were carried out with short columns relative to characteristic lengths. For example, Kozak et al. [36] compared their results with the experiments carried out by Bonsu [41] with soil columns of 96 mm in length. Bonsu [41] reported evaporation depths during stage 1 in the range of 10–20 mm for different soil samples. Based on the linear water content profile above the drying front and assuming an initially saturated water content of $\theta_s = 0.4$ m^3 m^{-3} with a residual water content of zero, the expected water loss for a front depth of $L = 96$ mm would be about $\frac{1}{2}\theta_s L = 19$ mm for media with $L_C > L$. The shallow evaporation depths reported by Bonsu [41] (10–20 mm) may be caused by small characteristic lengths $L_C < 96$ mm due to limiting hydraulic conductivity or narrow pore size distribution. But the reported shallow depths could also be explained by a drying front reaching the bottom of the sample during stage 1 and the following fragmentation of the liquid phase that breaks the liquid connections. Hence, it is unclear if the end of stage 1 is caused by small characteristic lengths or a too short sample length. The characteristic lengths for the soils presented in Fig. 11 are generally larger than the column lengths used by Bonsu [41], and only soils with pore size parameter $n > 2.8$ and $n < 1.3$ have characteristic lengths shorter than 96 mm for a potential drying rate of 10 mm day^{-1}. For intermediate values for n, predictions of stage 1 cannot be compared with these experimental results.

In the following, we compare the predicted characteristic length L_C with results obtained by lysimeter studies or long

laboratory columns. Jalota and Prihar [42] analyzed the effect of texture on evaporative drying for columns of 950 mm in length with potential drying rates between 6.3 and 15 mm day^{-1}. From the cumulative evaporation reported in their Fig. 2, we can estimate water loss during stage 1. Evaporation depths of 80, 50, and 15 mm for "silt loam," "sandy loam," and "loamy sand" are deduced. However, these values may also be affected by different initial water contents for the three columns. Jalota and Prihar [42] provide initial water contents, information on water retention, and bulk density that enable estimates of the drying front depth at the end of stage 1 for completely water-saturated initial conditions as explained in the previous subsection. The resulting front depths for the three soils are equal to 372, 435, and 135 mm for silt loam, sandy loam, and loamy sand. These values are compared in Fig. 12 with the characteristic lengths computed with Eqs. (20), (21), (24a), and (24b). While the front depths of the loamy sand and sandy loam are limited by the gravitational forces, the silt loam is affected by viscous effects as well. The measured values are in agreement with the range determined by the characteristic lengths. A lysimeter evaporation experiment with "clay loam" was carried out by Jackson et al. [43] and subsequently analyzed by Salvucci [44]. For initial evaporation rates between 2.5 and 9 mm per day, the transition from stage 1 to stage 2 occurred following cumulative evaporation of 15 mm of water. Based on the hydraulic parameters for clay loam given in Carsel and Parrish [40] an evaporation depth of 15 mm corresponds to a drying front depth of 95 mm as shown in Fig. 12 (the relatively shallow front depth is attributed to the dominance of viscous dissipation).

For Indio loam soil, Gardner and Hillel [45] measured drying rates for columns of length 220 and 1250 mm for potential drying rates ranging between 3 and 36 mm per day. From their results we estimated evaporation and drying front depths during stage 1. For the columns of 220 mm in length, the mass loss during stage 1 was rather constant (about 50% of the total water) for drying rates between 3.6 and
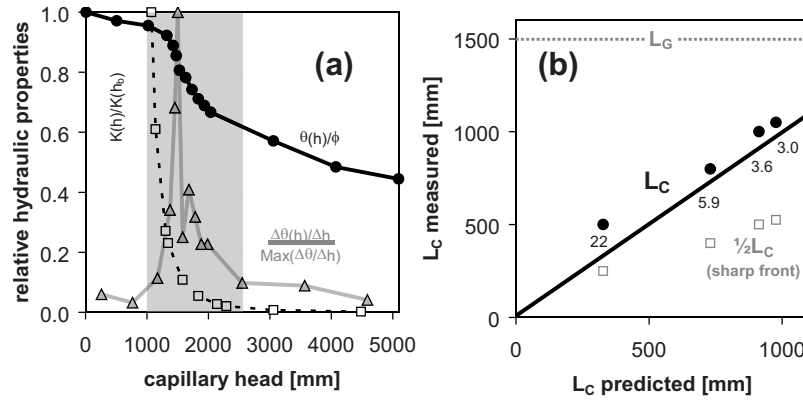
FIG. 13. Comparison between the experimental results of Gardner and Hillel [45] and predictions based on characteristic length estimates. (a) Hydraulic properties of the Indio loam [46] that were used to predict the characteristic length L_C. To show all relevant hydraulic properties within one figure, the water content was related to the porosity ϕ, the derivative $\Delta\theta/\Delta h$ was scaled by its maximum value, and the hydraulic conductivity was related to its value at air entry. The gray region indicates the maximum extent of the capillary driving force and characteristic length. (b) Gardner and Hillel [45] measured the evaporated mass for different potential drying rates using columns of 1250 mm in length. Potential drying rates e_0 (expressed in mm per day) are indicated by the numbers next to the symbols. The measured water loss during stage 1 decreased with increasing drying rate as predicted by characteristic length estimates. The black line indicates the 1:1 equivalence of the measured and predicted values of L_C. The measured and predicted characteristic lengths L_C are compared to L_G and a depth $d=\frac{1}{2}L_C$ (a sharp drying front with completely dry soil above the front) to highlight the effects of viscous dissipation and the existence of partially water-filled pore space above the front.

22 mm day^{-1}. For the long column, however, the total evaporated mass or evaporation depth increased with decreasing potential drying rate. We tried to reproduce these findings based on estimates of characteristic lengths derived from hydraulic functions for Indio loam provided by Mualem [46] and presented in Fig. 13(a). The air entry occurs at capillary head of 1000 mm, and above 2500 mm, the derivative $\Delta\theta/\Delta h$ becomes small and the hydraulic conductivity significantly diminishes. These changes above 2500 mm are interpreted as resulting from fragmentation of the liquid phase (breaking of thick films). The maximum capillary drive or characteristic length L_G is estimated as 2500 $-1000=1500$ mm (between air entrance and film disconnection). The hydraulic conductivity for this range (estimated by averaging measured values between 1030 and 2250 mm) is 5.6 mm day^{-1}. For this conductivity value the estimated characteristic lengths based on Eq. (20) are 975, 915, 730, and 330 mm for potential drying rates of 3.0, 3.6, 5.9, and 20 mm day^{-1}, respectively.

Based on Fig. 2 in [45] the water fraction evaporated in the first stage of evaporation was about 0.42, 0.40, 0.32, and 0.20 for potential drying rates of 3.0, 3.6, 5.9, and 20 mm day^{-1}. For a linearized water retention curve with zero residual water content and an initially saturated column with porosity 0.4 the estimated drying front depth L_C was 1050, 1000, 800, and 500 mm. These values are shown in Fig. 13(b) along with predictions based on theoretical characteristic lengths. Despite somewhat lower predictions than values deduced from Gardner and Hillel [45], the trends support our interpretation that the characteristic length provides reasonable estimates for the effects of soil texture on evaporative drying during stage 1 of the drying process. Now, the measured decrease of evaporated mass in stage 1 with increasing potential rate e_0 [45] can be explained with the increasing viscous dissipation. For the four analyzed drying

rates, the computed characteristic lengths are longer than the shorter column (220 mm) used by Gardner and Hillel [45]. This explains why no difference could be detected for the four drying rates because the drying front reached the bottom during stage 1 in all cases.

In Fig. 13(b) the gravitational length L_G and the depth $d=\frac{1}{2}L_C$ (corresponding to a front depth with no water above the drying front) are shown as well. Due to viscous dissipation, the front depth at end of stage 1 is smaller than L_G. If all water above the drying front would have been evaporated, the front depth for the measured data [45] would correspond to depths d that are much smaller than the predicted characteristic lengths L_C. The predicted values indicate that water remains above the drying front and the distribution is similar to the (linearized) water retention curve.

While our study of the role of soil textures was based on the water retention curve parametrized by the Van Genuchten model [27] the same analysis can be carried out by quantifying the width of the pore size distribution function. As revealed by Kosugi [47] and Assouline [48] for the Van Genuchten [27] and the Brooks-Corey [29] models, respectively, the width of the pore size distribution (expressed as standard deviation σ) decreases monotonically with increasing parameters n [27] and λ [29] of the water retention curve. Therefore the role of the width of the pore size distribution on the characteristic length can be deduced from the analysis based on the water retention parameter n. While we computed the characteristic lengths as a function of σ as well, we do not present the results because they just confirm the analysis based on the parameter n and no additional information can be deduced.

VI. SUMMARY AND CONCLUSIONS

During stage-1 drying, water evaporating from surface of an initially saturated porous medium is replaced by mass

flow from the invading drying front. We compare the roles of gravity, capillarity, and viscous dissipation and deduce characteristic lengths for the maximum extension of the hydraulically connected film region between the drying front and surface. The characteristic lengths depend on the size range between the smallest and largest pores within the film region. For media with large pore sizes, the characteristic length is dominated by gravity and capillarity and the viscous dissipation is negligible. For fine-textured media, viscous dissipation may limit the maximum hydraulically connected distance between the front and evaporating surface. We conducted simple drying experiments with two sands to determine the characteristic lengths and the extent of the film region. From theoretical and experimental results we deduce the following conclusions.

(i) For the analyzed sands, the mass of evaporated water during stage 1 was not dependent on potential evaporation rates. The high hydraulic conductivities of the sands did not limit liquid flow from the front to supply water at the surface.

(ii) The duration of stage 1 was controlled by the extent of the hydraulically connected film region. The extent of this region corresponds to a characteristic length defined by the pore size distribution of the porous medium. The extent of this film region determines the front depth at end of stage 1, and it was larger for the finer sand.

(iii) The capillary driving force for liquid flow during stage 1 defining a characteristic length is related to the width of the pore size distribution and not to the mean pore size. Characteristic lengths are estimated (*a priori*) by linearization of the water retention function, providing predictive capabilities for stage 1.

Enhancing the predictability of drying rates and water losses from porous media relies on an understanding of the controlling mechanisms. Future research efforts should focus on the following questions: effects of evaporation on liquid fragmentation and distribution above the drying front, mass exchange through the viscous boundary layer at the surface, and additional experimental verification of the role of pore size distribution and textural contrasts on drying behavior.

The validity of the linearization of the water retention curve and consequences on the assumed water content distribution above a drying front should be quantified in more detail. We have conducted preliminary experiments using the neutron transmission technique (at 100 μm resolution) and synchrotron x-ray tomography (7 μm) to measure the details of the water content distribution and connectivity, lending support to the linearized representation in sands (details will be reported in a forthcoming publication).

The effect of mass exchange at the evaporating surface with overlying viscous boundary layer is dependent on the air flow velocity and water content distribution at the surface as analyzed by Suzuki and Maeda [6] and Schlünder [7]. This additional potential source of resistance which lies at the interface between porous media and atmosphere is often confusing and erroneously attributed to limitations in porous media transport properties. Even following an extensive review by Van Brakel [1] the impact of surface water content on evaporation behavior remains unclear and deserves additional study. The working hypothesis concerning the extent of the hydraulically connected zone spanned by the pore size distribution and deduced from linearization of the water retention curves of two sands requires tests with different porous media, especially those that might introduce viscous limitations.

[1] J. Van Brakel, in *Advances in Drying*, edited by A. S. Mujumdar (Hemisphere, New York, 1980), Vol. 1, p. 217.

[2] M. Prat, Chem. Eng. J. **86**, 153 (2002).

[3] T. K. Sherwood, Ind. Eng. Chem. **22**, 132 (1930).

[4] J. R. Philip, J. Meteorol. **14**, 354 (1957).

[5] R. J. Idso, R. D. Reginato, R. D. Jackson, B. A. Kimball, and F. S. Nakagama, Soil Sci. Soc. Am. Proc. **38**, 831 (1974).

[6] S. Suzuki and S. Maeda, J. Chem. Eng. Jpn. **1**, 26 (1968).

[7] E.-U. Schlünder, Chem. Eng. Sci. **43**, 2685 (1988).

[8] A. G. Yiotis, I. N. Tsimpanogiannis, A. K. Stubos, and Y. C. Yortsos, Water Resour. Res. **43**, W06403 (2007).

[9] Y. Le Bray and M. Prat, Int. J. Heat Mass Transfer **42**, 4207 (1999).

[10] A. G. Yiotis, I. N. Tsimpanogiannis, A. K. Stubos, and Y. C. Yortsos, J. Colloid Interface Sci. **297**, 738 (2006).

[11] A. G. Yiotis, A. G. Boudouvis, A. K. Stubos, I. N. Tsimpanogiannis, and Y. C. Yortsos, Phys. Rev. E **68**, 037303 (2003).

[12] T. M. Shaw, Phys. Rev. Lett. **59**, 1671 (1987).

[13] J. B. Laurindo and M. Prat, Chem. Eng. Sci. **51**, 5171 (1996).

[14] Y. C. Yortsos, B. Xu, and D. Salin, Phys. Rev. Lett. **79**, 4581 (1997).

[15] B. Xu, Y. C. Yortsos, and D. Salin, Phys. Rev. E **57**, 739 (1998).

[16] H. Auradou, K. J. Måløy, J. Schmittbuhl, A. Hansen, and D. Bideau, Phys. Rev. E **60**, 7224 (1999).

[17] Y. Méheust, G. Løvoll, K. J. Måløy, and J. Schmittbuhl, Phys. Rev. E **66**, 051603 (2002).

[18] D. Or, Adv. Water Resour. (to be published).

[19] M. Tuller and D. Or, Water Resour. Res. **37**, 1257 (2001).

[20] A. G. Yiotis, A. K. Stubos, A. G. Boudouvis, I. N. Tsimpanogiannis, and Y. C. Yortsos, Transp. Porous Media **58**, 63 (2005).

[21] J. C. T. Eijkel, B. Dan, H. W. Reemeijer, D. C. Hermes, J. G. Bomer, and A. van den Berg, Phys. Rev. Lett. **95**, 256107 (2005).

[22] G. W. Scherer, J. Am. Ceram. Soc. **73**, 3 (1990).

[23] A. G. Yiotis, A. K. Stubos, A. G. Boudouvis, and Y. C. Yortsos, Adv. Water Resour. **24**, 439 (2001).

[24] P. Coussot, Eur. Phys. J. B **15**, 557 (2000).

[25] M. Prat and F. Bouleux, Phys. Rev. E **60**, 5647 (1999).

[26] T. Metzger and E. Tsotsas, Drying Technol. **23**, 1797 (2005).

[27] M. Th. Van Genuchten, Soil Sci. Soc. Am. J. **44**, 892 (1980).

[28] Y. Mualem, Water Resour. Res. **12**, 513 (1976).

[29] R. H. Brooks and A. T. Corey, J. Irrig. and Drain. Div. **92**, 61 (1966).

[30] E. Shimojima, A. A. Curtis, and J. V. Turner, J. Hydrol. **117**, 15 (1990).

[31] N. Ursino and T. Gimmi, Water Resour. Res. **40**, W01514 (2004).

[32] P. Lehmann, P. Wyss, A. Flisch, E. Lehmann, P. Vontobel, M. Krafczyk, A. Kaestner, F. Beckmann, A. Gygi, and H. Flühler, Vadose Zone J. **5**, 80 (2006).

[33] A. Klute and C. Dirksen, in *Methods of Soil Analysis*, edited by A. Klute, Agronomy Monograph No. 9 (ASA and SSSA, Madison, WI, 1986), Pt. 1, p. 687.

[34] A. A. Van de Griend and M. Owe, Water Resour. Res. **30**, 181 (1994).

[35] G. W. Scherer and D. M. Smith, J. Non-Cryst. Solids **189**, 197 (1995).

[36] J. A. Kozak, L. R. Ahuja, L. Ma, and T. R. Green, Vadose Zone J. **4**, 418 (2005).

[37] L. A. Richards, Physics (N.Y.) **1**, 318 (1931).

[38] W. J. Rawls, D. L. Brakensiek, and K. E. Saxton, Trans. ASAE **25**, 1316 (1982).

[39] J. Simunek, M. Th. Van Genuchten, and M. Sejna, HYDRUS software series No. 1, University of California, Riverside, 2005.

[40] R. F. Carsel and R. S. Parrish, Water Resour. Res. **24**, 755 (1988).

[41] M. Bonsu, Agric. Water Manage. **33**, 87 (1997).

[42] S. K. Jalota and S. S. Prihar, Aust. J. Soil Res. **24**, 357 (1986).

[43] R. D. Jackson, S. B. Idso, and R. J. Reginato, Water Resour. Res. **12**, 23 (1976).

[44] G. D. Salvucci, Water Resour. Res. **33**, 111 (1997).

[45] W. R. Gardner and D. I. Hillel, J. Geophys. Res. **67**, 4319 (1962).

[46] Y. Mualem, *Catalogue of the Hydraulic Properties of Unsaturated Soils* (Technion–Israel Institute of Technology, Haifa, Israel, 1974).

[47] K. Kosugi, Water Resour. Res. **30**, 891 (1994).

[48] S. Assouline, Water Resour. Res. **41**, W07019 (2005).